Histidine Self-assembly and Stability on Mineral Surfaces as a Model of Prebiotic Chemical Evolution: An Experimental and Computational Approach

D. Madrigal-Trejo[1,2] · P.S. Villanueva-Barragán[1,2] · R. Zamudio-Ramírez[1,2] ·
K. E. Cervantes-de la Cruz[1,3] · I. Mejía-Luna[1] · E. Chacón-Baca[4] ·
A. Negrón-Mendoza[2] · S. Ramos-Bernal[3] · A. Heredia-Barbero[2]

Abstract

The abiotic synthesis of histidine under experimental prebiotic conditions has proven to be chemically promising and plausible. Within this context, the present results suggest that histidine amino acid may function as a simple prebiotic catalyst able to enhance amino acid polymerization. This work describes an experimental and computational approach to the self-assembly and stabilization of DL-histidine on mineral surfaces using antigorite $((Mg, Fe)_3Si_2O_5(OH)_4)$, pyrite ($FeS_2$), and aragonite ($CaCO_3$) as representative minerals of prebiotic scenarios, such as meteorites, and subaerial and submarine hydrothermal systems. Experimental results were obtained through polarized-light microscopy, IR spectroscopy (ATR-FTIR), and differential scanning calorimetry (DSC). Molecular dynamics was performed through computational simulations with the MM + method in HyperChem software. IR spectra suggest the presence of peptide bonds in the antigorite-histidine and aragonite-histidine assemblages with the presence of amide I and amide II vibration bands. The FTIR second derivative inspection supports this observation. Moreover, DSC data shows histidine stabilization in the presence of antigorite and aragonite by changes in histidine thermodynamic properties, particularly an increase in histidine decomposition temperature (272ºC in antigorite and 275ºC in aragonite). Results from molecular dynamics are consistent with DSC data, suggesting an antigorite-histidine closer interaction with decreased molecular distances (*cca.* 5.5 Å) between the amino acid and the crystal surface. On the whole, the experimental and computational outcomes support the role of mineral surfaces in prebiotic chemical evolution as enhancers of organic stability.

Keywords Prebiotic synthesis · Organic catalyst · Peptide bond · Infrared spectroscopy · Differential scanning calorimetry · Molecular dynamics

✉ A. Heredia-Barbero
  aheredia@nucleares.unam.mx

Extended author information available on the last page of the article

Introduction

Histidine is a proteinogenic alpha-amino acid with an imidazole side chain that makes it a crucial catalytic molecule. Because the imidazole group has a pKa of approximately 6, histidine amino acid residues change electrical charge with subtle changes in pH; hence, they act as a general acid–base catalyst in proton transfer. Therefore, histidine is an essential amino acid in a large group of enzymes (Bender 2012; Nelson et al. 2017) and possibly was so in the early Earth.

The mechanisms by which the quasi-universal genetic code was established are still under debate. A series of diverse hypotheses suggest the order in which specific codons, and therefore amino acids, were incorporated into the genetic code (for an in-depth review, see Kun and Radványi 2018). Histidine has not been found in meteorites (Koga and Naraoka 2017), suggesting that this biomolecule must have been formed under early Earth conditions (Kitadai and Murayama 2018; Alifano et al. 1996; Baisuk and Navarro-González 1996). Moreover, it has been experimentally shown that plausible reaction mechanisms under prebiotic conditions could have resulted in the formation of histidine and imidazole derivatives, such as 1) synthesis of imidazole derivatives from formaldehyde, glyoxal, and ammonia (Oró et al. 1984); 2) the reaction between erythrose and formamidine to form imidazole-4-acetaldehyde and imidazole-4-glycol (Shen et al. 1987); and 3) the role of imidazole-4-acetaldehyde as a reaction intermediate in the non-enzymatic route for histidine synthesis by the Strecker cyanohydrin synthesis (Shen et al. 1990b). Frenkel-Pinter et al. (2019) showed the extensive and efficient oligomerization of histidine and other proteinaceous amino acids over some non-proteinaceous cationic amino acids, suggesting a chemical selective basis for its incorporation in early stages of life. Furthermore, reactions between histidine, cyanamide, and 4-amine-5-imidazolecarboxamide might yield the histidyl-histidine (His-His) dipeptide (Shen et al. 1990a). His-His dipeptide is a functional molecule capable of catalyzing the peptide-bond formation in the oligomerization of glycine as well as stimulating reactions with the participation of nucleotide derivatives and oligonucleotides (Shen et al. 1990a). L-dipeptides of serine-histidine (Ser-His) also have been shown to promote oligomerization of RNA by a transamination mechanism (Wieczorek et al. 2013).

These are some examples that suggest the relevance of small peptides in the construction of biological systems (Alifano et al. 1996).

Chemical evolution on early Earth, a transition of increasing molecular complexity, holds an intimate relationship with the physicochemical environment in which it develops, particularly minerals and mineral surfaces, which are considered essential for the emergence of life on Earth and, perhaps, other planetary bodies (Russell and Ponce 2020). Mineral surfaces have an essential role in the self-assembly of simple organic compounds towards supramolecular complexes (Rimola et al. 2019). Self-assembly on mineral surfaces could be achieved through adsorption, acting as a mechanism to concentrate, select, and organize reactants (Hazen 2006) in conjunction with mineral catalytic properties in the synthesis and polymerization of nucleotides and amino acids (Maurel and Leclerc 2016; Mendoza-Torres et al. 2020). Furthermore, mineral surfaces might protect complex organic compounds from ultraviolet radiation and hydrolysis (Maurel and Leclerc 2016; Rimola et al. 2019); consequently, organic stability is increased, and therefore, molecular lifetimes are enhanced.

Among minerals with relevance in prebiotic models, pyrite (FeS_2) is the most abundant iron-sulfide mineral on Earth (Rickard and Luther 2007), and it might have been of wide

distribution on the early Earth (Poulton and Canfield 2011). The ubiquity of iron sulfides is also noticeable in subaerial and submarine hydrothermal systems deposits, such as black smokers (Martin et al. 2008). Their abundance extends beyond terrestrial limits with the presence of troilite (FeS) and other iron sulfides in meteorites, interplanetary, and interstellar dust (Rubin and Ma 2017). Pyrite properties on heterogeneous catalysis have suggested its role in the polymerization of simple organic molecules and its establishment in early metabolic routes (Wächtershäuser 1990) towards an autotrophic origin of life (Wächtershäuser 2007). By contrast, clay minerals from the serpentine subgroup, and carbonates such as calcite ($CaCO_3$), stand out for their properties in concentrating organic reactants and enhancing their stability (Hazen et al. 2001; Mendoza-Torres et al. 2020; Schrenk et al. 2013). These minerals possibly were also abundant in a variety of environments in early Earth, such as alkaline hydrothermal vents, which have been recognized as plausible sites for prebiotic chemistry and chemical evolution (Sojo et al. 2016). Driven by serpentinization processes, redox gradients lead to the formation of simple organic compounds (Martin et al. 2008; Russell et al. 2010; Russell and Ponce 2020). In these settings, meter-sized aragonite ($CaCO_3$) columns form when the hydrothermal activity is constant (Ludwig et al. 2006). Conversely, subaerial hydrothermal systems such as hot springs, have also been under the spotlight as prebiotic environments for chemical evolution (for an in-depth review, see Damer and Deamer 2020). Subaerial environments also show the common presence of serpentine minerals (Giampouras et al. 2019; McCaig et al. 2020) and carbonates (Renaut and Jones 2011; Chavagnac et al. 2013).

The present work focuses on the adsorption of histidine on mineral surfaces of antigorite (($Mg, Fe)_3Si_2O_5(OH)_4$), pyrite (FeS_2), and aragonite ($CaCO_3$) to determine thermodynamic and structural changes in these molecular systems through experimental and computational approaches. Classical experimental approaches such as polarized microscopy, infrared spectroscopy, and differential scanning calorimetry provide macroscopic information, whereas the computational methods provide details on the molecule organic-mineral interactions (Rimola et al. 2019).

Materials and Methods

Slow Crystallization Experimental Design and Setup

We used three kinds of mineral samples: antigorite (($Mg, Fe)_3Si_2O_5(OH)_4$) as the main component of a serpentinite sample from the Acatlán complex, Puebla, Mexico (Fig. 1a); pyrite (FeS_2) with a granular habit derived from ROMINMEX S.A de C.V (Atlixco, Puebla, Mexico) (Fig. 1b); and aragonite ($CaCO_3$) with hexagonal prismatic habit obtained

(a)   (b)   (c)

1 cm   1 cm   1 cm
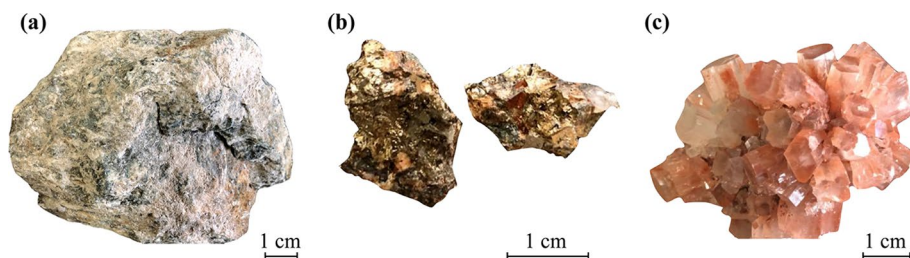
Fig. 1 Mineral samples employed: (**a**) antigorite; (**b**) pyrite; (**c**) aragonite

from Mineralia® (Coyoacán Centro, Ciudad de Mexico) (Fig. 1c). Mineral samples were washed under distilled water before crushing in an agate mortar. Once the minerals were ground (agate mortar), samples were washed with acetone (Sigma-Aldrich, St. Louis, Missouri, USA, purity > 99.5%) to clean the organic remains that might interfere with results interpretation. Each mineral sample was subject to three washing cycles. Afterwards, samples were dried in Petri dishes in a fume hood for seven days to avoid contamination.

A 100 μL saturated DL-histidine (Sigma-Aldrich, St. Louis, Missouri, USA, purity grade 98.5%) distilled water solution (45.6 mg of DL-histidine per 1 mL of distilled water) was added to Eppendorf tubes (1.5 mL) with antigorite (34.08 mg), aragonite (31.8 mg), and pyrite (160 mg). A parallel set was prepared for histidine control and corresponding minerals with no histidine as controls. In order to optimize the surface contact between the histidine solution and pulverized mineral sample, mixtures were done employing a vortex. The slow-crystallization experiments were carried out at room temperature (23ºC) in a fume hood up to evaporation, followed by a Polarized-light Microscopy, ATR-FTIR, and Differential Scanning Calorimetry (DSC) analyses.

Polarized-light Microscopy

For preliminary inspection between DL-histidine and the different mineral phases, a MOTIC BA310 POL Trinocular polarizing microscope (Motic®, China) was used with the following objective lenses: 4X/0.10, 10X/0.25, 40X/0.65-Spring, and 60X/0.80-Spring. A Moticam 10 camera with 10MP resolution was coupled to the microscope. Samples were studied with both parallel light and crossed-polarized light.

Attenuated Total Reflectance Infrared Spectroscopy (ATR-FTIR)

FT-IR spectra were obtained by using an ATR-FTIR PerkinElmer equipment with an accessory of universal sampling device ATR (spectrometer 100 FT-IR) and a zinc-selenide synthetic sample holder (ZnSe). Infrared absorption spectra were recorded in the $650–4000 \text{ cm}^{-1}$ range with a resolution of 4 cm^{-1} and four scans per sample. To increase the resolution of the FTIR spectra the second derivative method was applied to the amide II region (C-N stretching and N-H bend) (Angeles-Camacho et al. 2020). For detection and peak capture, we used Spectra software and exported data to Qtiplot (Bucarest, Romania) and Mathematica (Wolfram Research, Champaign, IL, USA) software for their further plotting and interpretation.

Differential Scanning Calorimetry (DSC)

For phase transition analyses, we employed a thermal system equipment DSC-100 Differential Scanning Calorimetry (Tryte Technology, HuNan Development Co. Ltd, Yuhua District, Changsha, Hunan, China). Temperature and crystallization enthalpy of samples were calibrated using pure water as standard. All samples were placed in clean aluminum holders (crucibles) followed by the addition of samples in the following amount: 36.4 mg of DL-histidine, 85.5 mg of pyrite, 85 mg of serpentine, 36.4 mg of aragonite, 47.2 mg of DL-histidine/pyrite, 30.1 mg of DL-histidine/serpentine and 43.1 mg of DL-histidine/ aragonite. A heating cycle was run until the temperature reached 500°C at a 10°C/min rate, under the air atmosphere. During the cooling cycle, no samples were analyzed because of the histidine decomposition during the warming cycle. Qtiplot (Bucarest, Romania) and

Mathematica (Wolfram Research, Champaign, IL, USA) softwares were used for the DSC plotting.

Computer Simulations: Geometry Optimization and Molecular Dynamics with the MM + method

A Hyperchem version 8.0.10 (Hypercube, Inc, Gainesville, FL, USA) program was used to perform geometry optimizations and molecular dynamics simulations. The structure of the organic molecules (the zwitterionic form of L-histidine) was obtained from the integrated library of the Hyperchem program, whilst the crystals (mineral phases) were obtained from the American Mineralogist Crystal Structure Database: aragonite (De Villiers 1971), pyrite (Bayliss 1977) and antigorite (Capitani and Mellini 2004). Crystal structures were processed and imported in CIF format for their subsequent edition in Avogadro (Avogadro Chemistry. Powered by Jekyll and Minimal Mistakes, https://avogadro.cc) as edited unit cell structures through the graphical interface of Hyperchem. Three histidine modules in a neutral state in association with the minimal crystalline structure for each mineral was built.

Before a Molecular Dynamics (MD) simulation, the geometry of the histidine-mineral system was previously optimized during three cycles, and a 2 ps MD simulation was performed in order to determine the coordinates of molecular structures in which the potential energy presents a minimal value. The complete geometry optimization was performed with the next configuration: a force field for MM + using a Polak–Ribiere conjugate gradient algorithm and the gradient from the quadratic mean of 0.0001 kcal·$Å^{-1}$·mol^{-1}, followed by a short MD of 1 ps in a vacuum. Finally, for each system, a 180 ps vacuum molecular dynamics simulation was run. The 180 ps simulation was coupled with a heating cycle of initial temperature of 290 K, final temperature of 873 K, step temperature of 2 K, run time of 100 ps, and cooling time of 40 ps with a step size of 1×10^{-5} ps.

Results

Polarized-light Microscopy

We identify histidine crystals by their anisotropy in the histidine control under polarized light microscopy with crossed Nicols. Histidine monocrystals show a prismatic (Fig. 2a) and acicular habit (Fig. 2b). Without considering chromatic aberrations they exhibit first-order interference colors. The association between histidine and mineral surfaces shows no visible histidine crystals in contrast with the histidine controls. The antigorite-histidine association shows translucent minerals whereas the pyrite-histidine sample shows opaque crystals with other mineral inclusions, either as micro-aggregates or nano-aggregates. Despite the microscopic resolution of mineral associations are not completely clear, the aragonite-histidine association exhibits a granular texture with submicrometer-sized euhedral crystals. The irregularity of thickness of the samples generated chromatic aberrations that prevented a further petrographic and mineralogical analysis.

Attenuated Total Reflectance Infrared Spectroscopy (ATR-FTIR)

The transmittance IR spectra display the histidine, mineral samples, and mineral-organic signals for the assemblies. The absorbance spectra were characterized through the
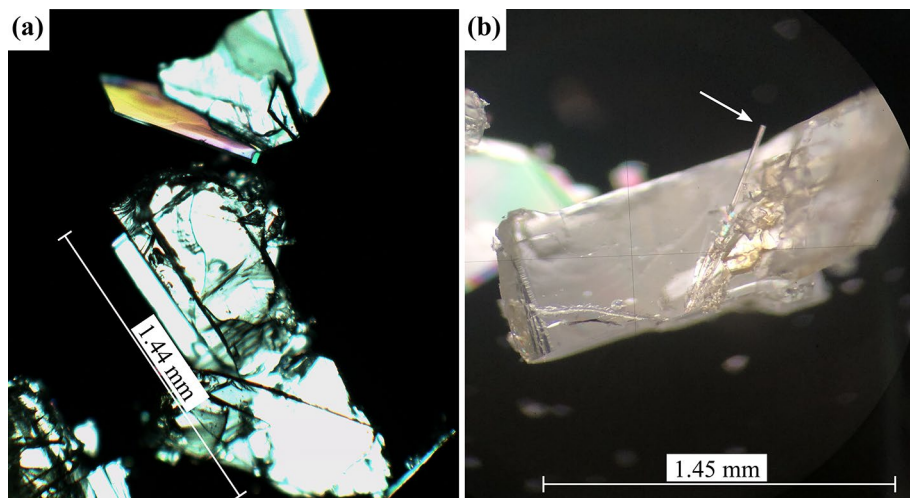
Fig. 2 Photomicrographs under crossed polarized light of histidine crystals (400× magnification). (**a**) Prismatic crystallization of histidine with a first-order interference color, (**b**) Visible acicular crystallization of histidine (white arrow)

molecular vibration modes of the bands against published references. The histidine control (Fig. 3a) presents a region between 3500 cm^{-1} and 2600 cm^{-1} associated with carboxylic acids, while the band located at 3290 cm^{-1} is due to N–H stretching of the imidazole group. Additionally, the band at *cca.* 1497 cm^{-1} originates from the vibration of the NH$_2$ group. The C–C stretching mode is seen at 1341 cm^{-1}, while the C-N stretching vibration mode is found at 1171 cm^{-1} (Viruthagiri et al. 2013). Histidine spectra also show an absorption peak at 1063 cm^{-1} associated with the in-plane C-H vibration. Bands in the region between 851 cm^{-1} and 805 cm^{-1} are related to C-N vibration, while the deformation of the imidazole ring occurs at the 833 cm^{-1} peak. The deformation of the chemical group C=O is identified by the bands at 1631 cm^{-1} and 683 cm^{-1}. Likewise, the band at 1111 cm^{-1} corresponds to the N–H group. Additionally, we attribute bands present at 1660 cm^{-1} and 1588 cm^{-1} to C=O and C-N stretching modes, respectively. This region is close to the region for the amide I and amide II signals, regions in which peptide bonds are detected. The stretching band at 1084 cm^{-1} is due to C–C-N stretching bonds (Viruthagiri et al. 2013).

In the IR spectrum obtained from the antigorite (Fig. 3b), a noticeable complex of bands derived from the asymmetric and symmetric Si–O-Si stretching modes can be observed in the 1200 cm^{-1} up to 650 cm^{-1} range (Crespo et al. 2019). In the spectrum of the antigorite-histidine sample (Fig. 3e), weak bands are seen in the 3200–2800 cm^{-1} region. Those bands are attributed to water molecules adsorbed on the surface of the silicate or to -OH groups from the silicon tetrahedra (González et al. 2017). In turn, at 1630 cm^{-1}, the presence of a band associated with the stretching in the C=O bond is observed (Di Foggia et al. 2012). Bands between 1400 cm^{-1} to 1500 cm^{-1} may be related to small contributions of CO in the plane and/or the C–C stretching vibration (Barth 2007). Likewise, in the region of 1700 cm^{-1} to 1600 cm^{-1}, the vibration of the amide band I is possibly present since signals are observed at approximately 1630 cm^{-1} and 1660 cm^{-1} due to the C=O bond tension and a slight signal at 1480–1545 cm^{-1} possibly caused by the bending of the
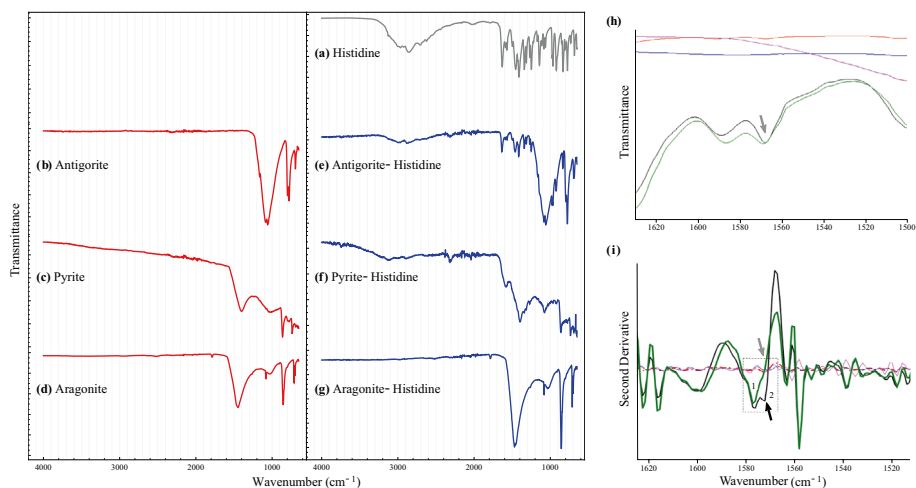
Fig. 3 ATR-FTIR spectra of: (**a**) histidine, (**b**) antigorite, (**c**) pyrite, and (**d**) aragonite crystals, (**e**) antigorite-histidine, (**f**) pyrite-histidine, and (**g**) aragonite-histidine assemblies. (**h**) Detail of the amide II (C-N stretching and N–H bend) band region, and (**i**) second derivative of the amide II region showing the presence of the amide II band (gray and black arrows) in histidine after hydration-dehydration (2) in contrast with the control (1)

N–H bond and C-N stretching vibration corresponding to amide II (Singh 2000; Barraza et al. 2013). At approximately 950 cm^{-1} possibly an N–H vibration is found (Barth 2007).

In the IR spectrum of pyrite (Fig. 3c), the observed bands around 1200–1000 cm^{-1} are related to the iron-sulfur bonds in pyrite (Fe=S) (De Oliveira et al. 2018). For the pyrite-histidine sample (Fig. 3f), it is possible to appreciate at *cca.* around 1400 cm^{-1} the symmetric COO stretching vibration of the carboxyl group (Di Foggia et al. 2012). This region may be associated with the N–H vibration (Barth 2007). In the region of 1690 cm^{-1} up to 1640 cm^{-1}, a band possibly generated either from the deformation of NH bonds or from the possible formation of peptide bonds (in the range of 1695 cm^{-1} to 1630 cm^{-1} the amide I band corresponds to the C=O chemical group) is seen (Di Foggia et al. 2012). As stated before, this analysis is not straightforward because -OH vibrations from water usually appear in this region (Singh 2000).

In aragonite (CaCO$_3$) the bands close to 1500 cm^{-1} and to 1400 cm^{-1} (strong) and between 900 cm^{-1} and 870 cm^{-1} are found. Also, other bands at 1082 cm^{-1}, and between 760 cm^{-1} to 710 cm^{-1} (weak) were observed (Ostrooumov 2007). A displacement similar to the CO group of cerussite-aragonite is seen from 840 cm^{-1} to 860 cm^{-1}. These bands correspond to the characteristic vibrations of the resonant triangular group CO$_3{}^{2-}$ seen in the infrared spectra of the aragonite (Fig. 3d) (Chakrabarty and Mahapatra 1999). Concerning the aragonite-histidine sample (Fig. 3g), the band around 1400 cm^{-1} from the carboxyl group exhibits the symmetric stretching vibration of COO. This band is sharpened by the amide II band which is located in the region from 1560 cm^{-1} to 1510 cm^{-1} (Di Foggia et al. 2012).

In the second derivative plot, amide, I and II vibrational transitions are clearer. Although the specific imidazole FTIR signals of the histidine are complex (amide I vibration reflect the protonation/deprotonation degree) we show that the second derivative performs a

detailed projection of the amides (Mesu et al. 2005). This analysis suggests the presence of underlying structural features such as peptide bonds after the hydration-dehydration processes (Ghosh et al. 2014). The different mineral samples present only the inorganic bands at different wavenumbers although the aragonite mineral presents similar bands to the carboxyl group (COO⁻) (not shown).

Differential Scanning Calorimetry (DSC)

From the thermograms, it is possible to identify that the histidine controls (Fig. 4a) presented two endothermic phase changes. Endothermic peaks are indicative that the products of the reaction have more potential energy than the reactants. The first phase change appeared at 170 °C, probably due to the melting and dehydration of the amino acid, while the second phase change was at 261 °C, which is an approximate value for the decomposition temperature of histidine (287 ºC) and presents an enthalpy change of $\Delta H = 50.9521$ J/g. These results show that histidine decomposes thermally but does not sublimate or melt (Weiss et al. 2018).

The thermogram of the antigorite mineral (Fig. 4b) shows the thermal decomposition starting at 60 °C that corresponds to the possible evaporation of water molecules included in the crystal planes. On the antigorite-histidine thermogram (Fig. 4e), an apparent fusion can be seen in the glass transition (Tv) (TA Instruments 2020) followed by the decomposition of the organic compound. The transitions such as the one shown between 80–100 °C, stand out for an enthalpy difference of $\Delta H = 0.3505$ J/g, which can be attributed to an endothermic reaction. Endothermal transitions starting at around 272 ºC, suggest a histidine breakdown. Furthermore, we attribute the transitions between 300–350 °C and beyond to subsequent steps in histidine decomposition.

In pyrite thermograms, it seems that this mineral interferes with the oxidation of the histidine. The thermal evolution of pyrite is complex, given the thermal decomposition and dissociation. The most remarkable feature of the presence of pyrite in the pyrite-histidine system is a strongly exothermic reaction in the range of 400 ºC up to 550 °C, attributed to a loss of mass as described already in other studies (Labus 2017). The thermal behavior of pyrite

Fig. 4 DSC thermograms of: (**a**) histidine, (**b**) antigorite, (**c**) pyrite, (**d**) aragonite, (**e**) antigorite-histidine sample, (**f**) pyrite-histidine sample, (**g**) aragonite-histidine samples
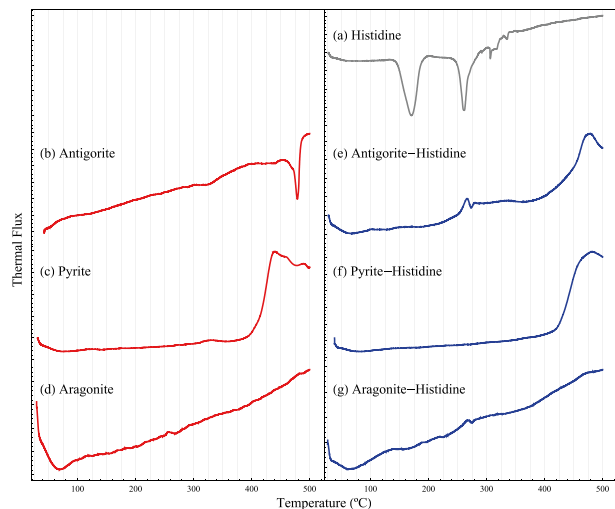
(Fig. 4c) and pyrite-histidine (Fig. 4f) are initially similar. A clear difference in the thermal behavior starting at 400 ºC is shown by an exothermic peak at 475 ºC in the pyrite-histidine sample, whereas the pyrite thermogram displays an exothermic peak close to 430 ºC.

The results with the aragonite (Fig. 4d) exhibit a different scenario, showing a series of alterations throughout the thermogram curve (Faust 1950). From room temperature up to 150 °C of the aragonite-histidine thermogram (Fig. 4g), the apparent "fusion" can be interpreted as a glass transition. Heating of the sample through its glass transition leads to the release of internal stress, therefore, the molecule transforms from a rigid structure to a flexible one on Tv. This possible molecular relaxation occurs as a weak endothermic transition (TA Instruments 2020). From 275 °C onwards, histidine proceeds to decompose presenting transitions such as a subtle one with an enthalpy difference of $\Delta H = 0.2895$ J/g.

During heating cycles with an upper limit up to 500 ºC, aragonite reaches the point where it decomposes into CO_2 gas and solid calcium oxide (CaO). The aragonite decomposition corresponds to an endothermic reaction (Stalport et al. 2007). In contrast, the lack of mineral decomposition reactions for the mineral phases of pyrite and antigorite reflects the stability of these inorganic compounds under high temperatures.

Computer Simulations: Geometry Optimization and Molecular Dynamics with the MM + method

The set of molecular dynamics simulations after geometry optimization step allows the relaxation of the optimized structures, thus obtaining the local energy minima for each mineral-organic system. Table 1 shows the total energies obtained from the geometry optimization cycles and molecular dynamics. Configurations of the systems after the molecular dynamics of 180 ps, as well as the evolution of the kinetic, potential, and total energy of the systems as a function of temperature, are shown in Fig. 5.

The results derived from molecular dynamics using the MM + method for 180 ps show that the total energy of the mineral-organic systems reaches values of 341 kcal mol^{-1} for the antigorite-histidine system, 302 kcal mol^{-1} for the aragonite-histidine system, and 257 kcal mol^{-1} for the pyrite-histidine system (Table 1). During the heating cycle, the antigorite-histidine system (Fig. 5a) kept organic molecules close to the antigorite surface (*cca*. 5.5 Å). In comparison, the pyrite-histidine (Fig. 5b) and aragonite-histidine (Fig. 5c) systems showed a greater distance between the mineral and organic molecules (*cca*. 752 Å and 352 Å, respectively). It should be noticed that histidine molecules in the aragonite-histidine system show similar orientations between them, whereas histidine molecules in antigorite-histidine and pyrite-histidine systems show no apparent order.

Table 1 Total energy for each mineral-organic system during geometry optimization cycles and molecular dynamics

Mineral-3 Histidine assemblies	1st geometry optimization (kcal mol^{-1})	2nd geometry optimization (kcal mol^{-1})	3rd geometry optimization (kcal mol^{-1})	Short molecular dynamics (kcal mol^{-1})	180 ps molecular dynamics (kcal mol^{-1})
Antigorite-histidine	23.91	22.94	22.97	23.11	341.52
Pyrite-histidine	26.80	23.87	23.68	23.55	256.76
Aragonite-histidine	11.90	12.60	12.67	12.33	302.20
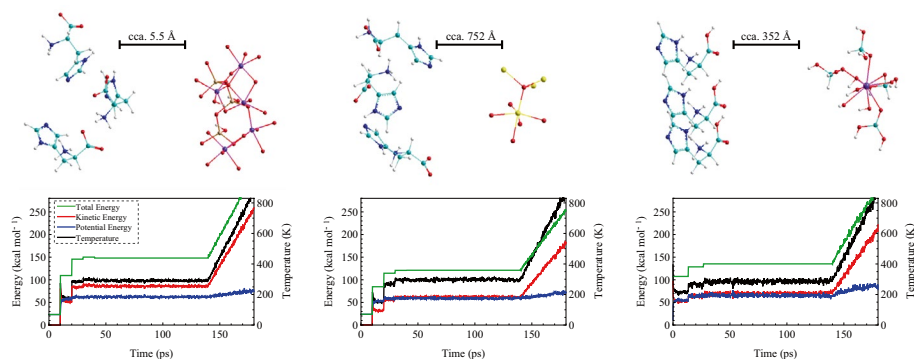
Fig. 5 Configuration of mineral-organic assemblies after molecular dynamics runs with the MM + method in addition to energy and temperature plots for (**a**) antigorite-histidine assembly, (**b**) pyrite-histidine assembly, (**c**) aragonite-histidine assembly

Discussion

Based on the present experimental data using polarized light microscopy, we find that none of the mineral-organic assemblies exhibit a visible histidine growth. Although there are no apparent histidine crystals on the mineral-organic assemblies, the IR spectra and DSC thermograms clearly show the occurrence of the histidine-mineral interaction.

IR spectra from the three mineral-organic samples show a series of bands in the range between 1700 cm^{-1} and 1500 cm^{-1}, in which peptide bond vibrations might be present (amide I and amide II vibrations). Nevertheless, amide I and amide II bands by themselves, are not a straightforward diagnostic for the presence of peptide bonds, since OH bonds in water molecules also present IR vibrations overlapping with amide I and II vibrations (Singh 2000). In this case, water molecules may be present as byproducts of peptide bond formation or perhaps OH radicals are present as an induced reaction between mineral and organic phases. Although the results here are not conclusive, the precipitation of histidine on mineral surfaces through slow crystallization suggests a peptide bond formation, particularly in the formation of histidyl-histidine dipeptide. A more detailed analysis of the second derivative signal of the amide II regions suggests the presence of peptide bonds after the hydration-dehydration processes. The complex FTIR signal of the histidine amino acid must be studied in more detail comparing the infrared signals and thermodynamic behavior through DSC thermograms. For instance, the FTIR band amide II at 1572 cm^{-1} agrees with the affinity between the antigorite to histidine.

Concerning the DSC thermograms, aragonite and antigorite mineral-organic assemblages show positive enthalpy changes, indicating endothermic reactions, whereas the pyrite-histidine sample shows no endothermal transitions. Differences between the breakdown temperature of histidine without mineral and histidine in aragonite-histidine and antigorite-histidine samples, highlight the prominent role of mineral surfaces in increasing the stability of organic compounds. As a mineral of the serpentine subgroup, antigorite is a weak heat conductor and may favor the interaction between amino acids and its mineral surface without destabilization by heating at certain temperatures.

Computational simulations employing molecular dynamics show that the antigorite-histidine interaction results in the least distance between organic molecules and its associated crystal structure, while interactions in aragonite-histidine and pyrite-histidine systems resulted in greater distances between the organic molecules and crystals. The

antigorite-histidine molecule-scale interaction is a matter of further research, nevertheless, computational and experimental results suggest a distinctive role of serpentine minerals (and clay minerals in general) in the stability and self-assembly of amino acids, as previously reported (Hazen and Sverjensky 2010; Hashizume 2012; Rimola et al. 2019).

Throughout the slow crystallization experiments performed, our findings support the Deamer-Damer hypothesis on a hot spring chemical evolution and prebiotic chemistry towards the origin of complex molecules relevant in life formation (Deamer and Damer 2017). The results here suggest that mineral surfaces might aid in increasing the complexity of molecular systems with relevance in the construction of molecular evolution events. Although the experimental design in this work is related to a hot spring environment with a wet-dry cycle, the minerals used in this work are also present in extraterrestrial objects such as meteorites. This fact opens the opportunity to research for self-assembly and stability properties of minerals under a pool of conditions, such as UV radiation, vacuum, high pressure, low/high pH, hydration-dehydration cycles, among others.

Conclusions

This work partially characterized the differential thermal response of the amino acid histidine to the interaction of different mineral surfaces. Preliminary IR spectroscopy data suggest the presence of peptide bonds at least at the antigorite-histidine assembly confirmed by using the second derivative method. Moreover, DSC data also suggest a stabilization of the histidine through the interaction with aragonite and antigorite, whereas pyrite had no apparent interaction with histidine under these conditions. These results support the perspective in which chemical evolution, particularly oligomerization of amino acids, developed within a set of diverse mineral surfaces present at a particular prebiotic environment, with different affinity and thermodynamic behavior by enhancing molecular stability. Molecular dynamics show small distances between antigorite and histidine molecules, which might give an insight into the molecular mechanism of peptide bond formation on the antigorite surface. Further experimental and computational research with variations in the experimental design and physical conditions will give more insight into plausible prebiotic environments from the organic-mineral stability and self-assembly perspective.

Declarations

Conflicts of Interest The authors have no conflicts of interest to declare that are relevant to the content of this article.

Ethics Approval We declare that our research was performed without cells, persons, or animal models.

Consent to Participate All authors contributed to the study conception and design of the present manuscript. all authors agreed with the content of this manuscript.

Consent for Publication All authors gave explicit consent to submit and publish this manuscript.

References

Alifano P, Fani R, Liò P, Lazcano A, Bazzicalupo M, Carlomagno MS, Bruni CB (1996) Histidine Bio-synthetic Pathway and Genes: Structure, Regulation, and Evolution. Microbiol Rev 60(1):44–69

Angeles-Camacho E, Cruz-Castañeda J, Meléndez A, Colín-García M, de la Cruz KC, Ramos-Bernal S, Negrón-Mendoza A, Garza-Ramos G, Rodríguez-Zamora P, Camargo-Raya C, Heredia A (2020) Potential Prebiotic Relevance of Glycine Single Crystals Enclosing Fluid Inclusions: An Experimental and Computer Simulation with Static Magnetic Fields. Advances in Biological Chemistry 10(5):140–156

Basiuk VA, Navarro-González R (1996) Possible role of volcanic ash-gas clouds in the Earth's prebiotic chemistry. Origins Life Evol Biosphere 26:173–194. https://doi.org/10.1007/BF0180985

Barraza-Garza G, de la Rosa LA, Martínez-Martínez A, Castillo-Michel H, Cotte M, Alvarez-Parrilla E (2013) La microscopía de infrarrojo con transformada de Fourier (FTIRM) en el estudio de sistemas biológicos. Revista latinoamericana de química 41(3):125–137

Barth A (2007) Infrared spectroscopy of proteins. Biochimica et Biophysica Acta - Bioenergetics 1767(9):1073–1101. https://doi.org/10.1016/j.bbabio.2007.06.004

Bender D (2012) *Amino acid metabolism*. 3th ed. John Wiley & Sons

Chakrabarty D, Mahapatra S (1999) Aragonite crystals with unconventional morphologies. J Mater Chem 9(11):2953–2957. https://doi.org/10.1039/a905407c

Chavagnac V, Ceuleneer G, Monnin C, Lansac B, Hoareau G, Boulart C (2013) Mineralogical assemblages forming at hyperalkaline warm springs hosted on ultramafic rocks: A case study of Oman and Ligurian ophiolites. Geochem Geophys Geosyst 14(7):2474–2495. https://doi.org/10.1002/ggge.20146

Crespo M, Pereira D, García M, Gallardo J and Escribano V (2019) Characterization of Serpentines from Different Regions by Transmission Electron Microscopy, X-ray Diffraction, BET Specific Surface Area and Vibrational and Electronic Spectroscopy. Fibers 7(47). https://doi.org/10.3390/fib7050047

Damer B, Deamer D (2020) The hot spring hypothesis for an origin of life. Astrobiology 20(4):429–452. https://doi.org/10.1089/ast.2019.2045

Deamer D, Damer B (2017) Can Life Begin on Enceladus? A Perspective from Hydrothermal Chemistry Astrobiology 17(9):834–839. https://doi.org/10.1089/ast.2016.1610

Faust GT (1950) Thermal analysis studies on carbonates; I. Aragonite and calcite American Mineralogist 35:207–224

Foggia M, Taddei P, Torreggiani A, Dettin M, Tinti A (2012) Self-assembling peptides for biomedical applications: IR and Raman spectroscopies for the study of secondary structure. Proteomics Research Journal 2(3):231–272

Frenkel-Pinter M, Haynes JW, Martin C, Petrov AS, Burcar BT, Krishnamurthy R, Hud NV, Leman LJ, Williams LD (2019) Selective incorporation of proteinaceous over nonproteinaceous cationic amino acids in model prebiotic oligomerization reactions. *Proceedings of the National Academy of Sciences* 116(33) 16338–16346. https://doi.org/10.1073/pnas.1904849116

Ghosh A, Tucker M, Gai F (2014) 2D IR Spectroscopy of Histidine: Probing Side-Chain Structure and Dynamics via Backbone Amide Vibrations. *The Journal of Physical Chemistry* 118(29). https://doi.org/10.1021/jp411901m

Giampouras M, Garrido CJ, Zwicker J, Vadillo I, Smrzka D, Bach W, Peckmann J, Jiménez P, Benavente J, García-Ruiz JM (2019) Geochemistry and mineralogy of serpentinization-driven hyperalkaline springs in the Ronda peridotites. Lithos 105215:350–351. https://doi.org/10.1016/j.lithos.2019.105215

González J, Rodríguez J, Tarazona JM, Luna D, Ríos C, García C, Castellanos O, Bonilla J, Pinto JL, Henao JA, Mendoza C, Mejía E, Cabanzo R, Molina D (2017) Caracterización Mineralógica, Química y Espectroscópica de la Serpentinita en la Cantera de Explotación de Córdoba (Quindío). Geología Norandina 2:19–39

Hashizume H (2012) Role of Clay Minerals in Chemical Evolution and the Origins of Life, in Clay Minerals in Nature - Their Characterization. Modification and Application 191–208. https://doi.org/10.5772/50172

Hazen RM (2006) Mineral surfaces and the prebiotic selection and organization of biomolecules. Am Miner 91:1715–1729. https://doi.org/10.2138/am.2006.2289

Hazen RM, Filley TR, Goodfriend GA (2001) Selective adsorption of L- and D-amino acids on calcite: Implications for biochemical homochirality. Proc Natl Acad Sci USA 98(10):5487–5490. https://doi.org/10.1073/pnas.101085998

Hazen RM, Sverjensky DA (2010) Mineral surfaces, geochemical complexities, and the origins of life. Cold Spring Harb Perspect Biol 2(5):a002162. https://doi.org/10.1101/cshperspect.a002162

Kitadai N, Maruyama S (2018) Origins of building blocks of life: A review. Geosci Front 9(4):1117–1153. https://doi.org/10.1016/j.gsf.2017.07.007

Koga T, Naraoka H (2017) A new family of extraterrestrial amino acids in the Murchison meteorite. Scientific Reports 7(1):1–8. https://doi.org/10.1038/s41598-017-00693-9

Kun Á, Radványi Á (2018) The evolution of the genetic code: Impasses and challenges. BioSystems 164:217–225. https://doi.org/10.1016/j.biosystems.2017.10.006

Labus M (2017) Thermal methods implementation in analysis of fine-grained rocks containing organic matter. J Therm Anal Calorim 129:965–973. https://doi.org/10.1007/s10973-017-6259-7

Ludwig KA, Kelley DS, Butterfield DA, Nelson BK, Früh-Green G (2006) Formation and evolution of carbonate chimneys at the Lost City Hydrothermal Field. Geochim Cosmochim Acta 20(4):90–99. https://doi.org/10.1016/j.gca.2006.04.016

Martin W, Baross J, Kelley D, Russell MJ (2008) Hydrothermal vents and the origin of life. Nat Rev Microbiol 6(11):805–814. https://doi.org/10.1038/nrmicro1991

Maurel MC, Leclerc F (2016) From foundation stones to life: Concepts and results. Elements 12(6):407–412. https://doi.org/10.2113/gselements.12.6.407

McCaig AM, Früh-Green GL, Kelemen P, Teagle DAH (2020) Serpentinite in the earth system. Philosophical Transactions of the Royal Society A: Mathematical, Physical and Engineering Sciences 378(2165):20190332. https://doi.org/10.1098/rsta.2019.0332

Mendoza-Torres E, Cruz-Catañeda J, Negrón-Mendoza A, Heredia A (2020) Computer and Experimental Simulation of Alloxazine Synthesis from Gamma Irradiation of Amino Acids on Iceland Spar: A Prebiotic Chemistry Perspective. J Mol Evol 88(3):284–291

Mesu JG, Visser T, Soulimani F, Weckhuysen BM (2005) Infrared and Raman spectroscopic study of pH-induced structural changes of L-histidine in aqueous environment. Vib Spectrosc 39(1):114–125

Nelson DL, Cox MM, Lehninger AL (2017) Lehninger principles of biochemistry, 7th edn. Freeman, W.H

Oliveira EM, Oliveira CM, Bauer Sala MV, Montedo ORK, Peterson M (2018) Thermal behavior of pyrite in the CO_2 and N_2 atmosphere for obtaining pyrrhotite: A magnetic material. Materials Research 21(6):e20170244. https://doi.org/10.1590/1980-5373-MR-2017-0244

Oró J, Basile B, Cortes S, Shen C, Yamrom T (1984) The prebiotic synthesis and catalytic role of imidazoles and other condensing agents. Orig Life 14(1–4):237–242. https://doi.org/10.1007/BF00933663

Ostrooumov M (2007) Espectrometría infrarroja de reflexión en Mineralogía Avanzada. Gemología y Arqueometría: Monografías del Instituto de Geofísica Universidad Nacional Autónoma de México 12(1):7–16

Poulton SW, Canfield DE (2011) Ferruginous conditions: a dominant feature of the ocean through Earth's history. Elements 7(2):107–112

Renaut R, Jones B (2011) Hydrothermal Environments, Terrestrial. Encyclopedia of Geobiology 467–479. https://doi.org/10.1007/978-1-4020-9212-1_114

Rickard D, Luther GW (2007) Chemistry of iron sulfides. Chem Rev 107(2):514–562

Rimola A, Sodupe M, Ugliengo P (2019) Role of mineral surfaces in prebiotic chemical evolution. silico quantum mechanical studies Life 9(1):10. https://doi.org/10.3390/life9010010

Rubin AE, Ma C (2017) Meteoritic minerals and their origins. Chem Erde 77(3):325–385. https://doi.org/10.1016/j.chemer.2017.01.005

Russell MJ, Hall AJ, Martin W (2010) Serpentinization as a source of energy at the origin of life. Geobiology 8(5):355–371. https://doi.org/10.1111/j.1472-4669.2010.00249.x

Russell MJ, Ponce A (2020) Six 'Must-Have ' Minerals for Life ' s Emergence : Fougerite and Mackinawite. Life 10(11):291. https://doi.org/10.3390/life10110291

Schrenk MO, Brazelton WJ, Lang SQ (2013) Serpentinization, carbon, and deep life. Rev Mineral Geochem 75(1):575–606. https://doi.org/10.2138/rmg.2013.75.18

Shen C, Mills T, Oró J (1990a) Prebiotic synthesis of histidyl-histidine. J Mol Evol 31(3):175–179. https://doi.org/10.1007/BF02109493

Shen C, Yang L, Miller SL, Oró J (1987) Prebiotic synthesis of imidazole-4-acetaldehyde and histidine. Orig Life Evol Biosph 17(3–4):295–305. https://doi.org/10.1007/BF02386469

Shen C, Yang L, Miller SL, Oró J (1990b) Prebiotic synthesis of histidine. J Mol Evol 31(3):167–174. https://doi.org/10.1007/BF02109492

Singh BR (2000) Basic aspects of the technique and applications of infrared spectroscopy of peptides and proteins. ACS Symp Ser 750:2–37. https://doi.org/10.1021/bk-2000-0750.ch001

Sojo V, Herschy B, Whicher A, Camprubí E, Lane N (2016) The Origin of Life in Alkaline Hydrothermal Vents. Astrobiology 16(2):181–197. https://doi.org/10.1089/ast.2015.1406

Stalport F, Coll P, Szopa C, Person A, Navarro-González R, Cabane M, Ausset P, Vaulay MJ (2007) Search for past life on Mars: Physical and chemical characterization of minerals of biotic and abiotic origin: 2. Aragonite Geophysical Research Letters 34:L24102. https://doi.org/10.1029/2007GL031184

TA Instruments (2020) How to Interpret the Unexpected Transitions in DSC Results. *AZoM*. Available at: https://www.azom.com/article.aspx?ArticleID=12101

Viruthagiri G, Praveen P, Mugundan S, Anbuvannan M (2013) Growth and Characterization of L-Histidine Doped Thiourea Single Crystals by Slow Evaporation Method. Indian Journal of Advances in Chemical Science 1(4):193–200

Wächtershäuser G (1990) Evolution of the first metabolic cycles. Proc Natl Acad Sci 87(1):200–204. https://doi.org/10.1073/pnas.87.1.200

Wächtershäuser G (2007) On the chemistry and evolution of the pioneer organism. Chem Biodivers 4(4):584–602. https://doi.org/10.1002/cbdv.200790052

Weiss IM, Muth C, Drumm R, Kirchner HOK (2018) Thermal decomposition of the amino acids glycine, cysteine, aspartic acid, asparagine, glutamic acid, glutamine, arginine and histidine. BMC Biophysics 11(1):2. https://doi.org/10.1186/s13628-018-0042-4

Wieczorek RD, Dörr M, Chotera, A, Luisi, PL, Monnard, PA (2013) Formation of RNA Phosphodiester Bond by Histidine-Containing Dipeptides. 14(2), 217–23. https://doi.org/10.1002/cbic.201200643

Authors and Affiliations

D. Madrigal-Trejo[1,2] · **P.S. Villanueva-Barragán[1,2]** · **R. Zamudio-Ramírez[1,2]** ·
K. E. Cervantes-de la Cruz[1,3] · **I. Mejía-Luna[1]** · **E. Chacón-Baca[4]** ·
A. Negrón-Mendoza[2] · **S. Ramos-Bernal[3]** · **A. Heredia-Barbero[2]**

[1]   Facultad de Ciencias, Departamento de Física, UNAM, Apdo. Postal 70-407, C.P. 04510 Ciudad Universitaria, Ciudad de México, México

[2]   Laboratorio de Evolución Química, Instituto de Ciencias Nucleares, Universidad Nacional Autónoma de México, Circuito Exterior S/N, Ciudad Universitaria Coyoacán, C.P. 04510 Ciudad de México, México

[3]   Departamento de Física de Plasmas e Interacción de Radiación con Materia, Instituto de Ciencias Nucleares, Universidad Nacional Autónoma de México, Circuito Exterior S/N, Ciudad Universitaria Coyoacán, C.P. 04510 Ciudad de México, México

[4]   Universidad Autónoma de Nuevo León, Facultad de Ciencias de la Tierra, Exhacienda de Guadalupe, Carretera a Cerro Prieto km 8, Linares, Nuevo León, C.P. 67700, México